THE EFFECT OF VORTEX GENERATORS ON ACTIVE BATTERY

THERMAL MANAGEMENT SYSTEMS

An Undergraduate Research Scholars Thesis

by

CARLOS FELIPE LOPEZ

Submitted to Honors and Undergraduate Research
Texas A&M University
in partial fulfillment of the requirements for the designation as

UNDERGRADUATE RESEARCH SCHOLAR

Approved by
Research Advisor: Dr. Partha P. Mukherjee

May 2013

Major: Mechanical Engineering

TABLE OF CONTENTS

ABSTRACT

The Effect of Vortex Generators on Active Battery Thermal Management Systems (May 2013)

Carlos Felipe Lopez
Department of Mechanical Engineering
Texas A&M University

Research Advisor: Dr. Partha P. Mukherjee
Department of
Mechanical Engineering

As a result of increasing oil prices and consumer environmental awareness, "green" products such as electric vehicles (EVs) have grown in popularity, but the energy storage technologies that make such products possible have many hurtles preventing further growth. Drawbacks such as battery safety issues, cycle related cost, and poor low temperature performance, all of which are thermally dependent, slow the growth of the emerging electric and hybrid electric vehicle (HEV) market. There are many improvements that can be made to the battery thermal management systems (BTMS) commonly used in EVs, including, but not limited to, the use of phase change materials and the addition of vortex generators in coolant flow channels. This study examines the effects of vortex generators on the heat transfer performance of typical battery thermal management solutions. Computational fluid dynamics simulation software designed for studying heat transfer problems in lithium-ion batteries was used to determine such effects. The addition of vortex generators to a generalized BTMS has shown an increase in average heat transfer coefficient of 38% and a decrease in average cell wall temperature of 6 Kelvin with a manageable increase in pressure cost.

ACKNOWLEDGEMENTS

NOMENCLATURE

EV   Electric Vehicle

HEV   Hybrid-Electric Vehicle

PHEV   Plug-in Hybrid-Electric Vehicle

Li-ion   Lithium-ion

NiMH   Nickel-metal hydride

NiCad   Nickel-cadmium

BTMS   Battery thermal management systems

BSM   Battery Simulation Module

BDS   Battery Design Studio$^{®}$

CFD   Computation Fluid Dynamics

CHAPTER I

INTRODUCTION

Motivation

Historically, the abundance of oil reserves and the demand for reliable transportation have caused a considerable global dependence on petrochemicals. However, the petroleum market has become increasingly dynamic due to the effect of environmental restrictions and the political nature of the industry. Previous attempts to alleviate oil dependence have proven not to be commercially viable, particularly in the areas of personal transportation and energy storage. One strong alternative to petroleum based transportation are electric vehicles, or EVs, where recent advancements in battery technology have driven a slow adoption. Many different rechargeable battery designs exist but only a few meet the criteria for use in EVs or Hybrid Electric Vehicles (HEVs). Excess heat generated from the electrochemical reaction in the batteries is a primary mode of failure for these systems. Ideally, this heat would be transferred away from the batteries as fast as possible to improve the lifetime and performance of HEV batteries. This thermal management issue needs to be addressed if electric vehicles are to remain competitive in a petroleum market.

Background

Much of the current research on batteries for vehicle applications is focus on improving performance (cycle life, power, and specific energy) by careful selection of electrode materials and configuration. For example, lithium-ion cells are the clear choice for use in personal electronics because of the technology's high specific energy and energy density compared to nickel-cadmium (NiCad) and nickel-metal hydride (NiMH) batteries. This is not the case

however, in HEVs, as NiMH still dominate, despite li-ion batteries having nearly twice the specific energy and energy density [1].

The benefits of using li-ion batteries for HEV applications are not without drawbacks, however. Some key issues with using li-ion batteries in EVs include safety, cost, and poor performance in low temperature operations [2]. All of these issues can be addressed by appropriate battery thermal management systems (BTMS). Only a small research effort is focused on improving the thermal performance of EV batteries. Some important aspects to the study of battery thermal management, particularly for lithium-ion cells, include the effect of temperature on capacity fade, thermal runaway, and cold temperature performance [3].

There are many active thermal management systems that vary in design depending on the application. However, the systems can be grouped into a few separate categories based on the type of working fluid: air, coolant, or phase change material (PCM). Solutions that implement air and liquid coolants are considered to be active systems because they require the use of a blower or other flow distributers. Because air has a relatively low heat capacity and conductivity, liquid cooling might be preferred, with many different coolants available [2]. The cost of using liquid over air-cooling is the added complexity of the liquid cooling system, as it needs to be recirculated using pumps whereas air does not and can be drawn from the cabin. Passive thermal management, or that which uses a PCM, is a promising alternative, as the material can undergo a phase change under more extreme conditions, capturing excess heat and lowering the number of hotspots and the chance of thermal runaway [3,4].

While there are many studies that address the nuances both of active and passive cooling, few are researching the effects of vortex generators on the heat transfer efficiency of active or even

passive BTMS. Vortex generators have been studied extensively in a general context with the goal of promoting turbulent or laminar mixing to increase the effective rate of heat transfer at a head pressure cost [5]. The aim of my studies is to determine the effect of vortex generators on the performance of battery thermal management systems in electric vehicles. The key concept to improving the performance of BTMS is to find the balance between rate of heat transfer, and pressure cost, both of which are dependent on the turbulence of the coolant flow.

CHAPTER II

METHODOLOGY

Lithium Ion Batteries

A battery consists of two electrodes, an anode and a cathode, with a porous separator in between. The electrolyte separator is an electrical insulator but ion conductor. This allows electrons to flow from the anode through the load and back to the cathode, while ions to do the reverse across the separator [6]. Modern rechargeable lithium ion batteries typically use carbon for the negative electrode, a lithium metal oxide for the positive, and a lithium salt in an organic solvent for the separator, but the exact materials vary. The electrode and separator microstructures depend on the materials chosen and vary in design, from simple two dimensional layers to complex three dimensional architectures, while the macrostructures remain relatively standard.

Construction

A battery cell consists of a single set of anode, cathode, and separator, with positive and negative connectors. Several battery cells are combined to form a battery module, which can then be combined to form a battery pack. The two most common types of battery cell structures are stacked (flat-plate) and spiral-wound (cylindrical) though there are other configurations such as bobbin and bipolar plate [8]. Stacked cells are more practical in electric vehicle applications due to the greater energy density and packing efficiency associated with the design, among other advantages. However, the lack of ample space between the battery modules in typical stacked packages can cause overheating problems due to the lack of coolant flow between casings [9]. Figure 1 shows the construction of a stacked battery module including the individual flat plate cells, connector tabs, and packaging.
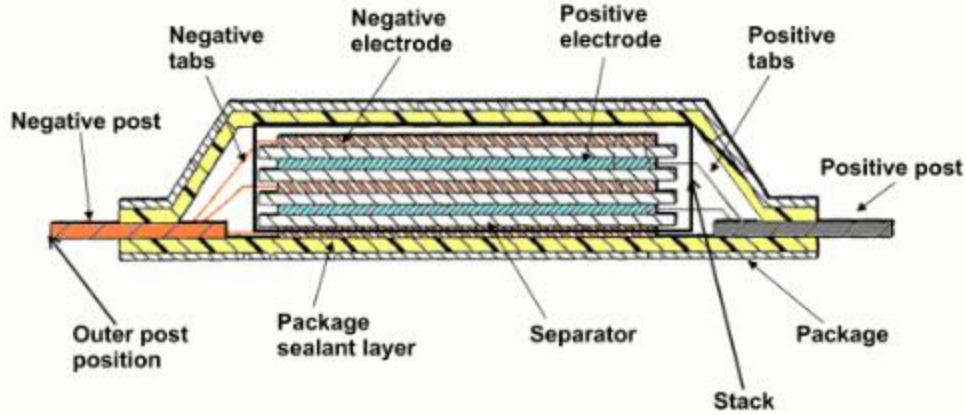
Figure 1. Typical macro-structure of a battery module made from stacked cells. [7]

Electrochemistry

The anode and the cathode are both porous structures, permitting the insertion and extraction of lithium ions to and from the electrode crystal lattice. During discharge, the lithium ions migrate from the anode to the cathode with the reverse process during charging [9]. For a lithium cobalt-oxide electrode, the reaction at the positive electrode is

$$Li^+ + e^- + CoO_2 \leftrightarrow LiCoO_2 \tag{1}$$
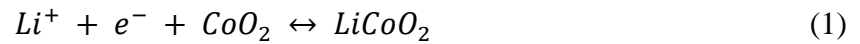
and the reaction at the negative electrode is

$$Li^+ + e^- + C_6 \leftrightarrow LiC_6 . \tag{2}$$

The most commonly used electrochemical model is one developed by Doyle, Fuller, and Newman [10] with the equation form used by Thomas, Newman, and Darling [11]. Solid and solution phase potentials and concentrations along with solution phase current and reaction rate are modeled by Equations 3 through 8 and solved numerically using Crank-Nicolson and Newton-Raphson methods [12].

$$i_n = i_o \left[\exp\left(\frac{\alpha_a F\left(\Phi_1 - \Phi_2 - U - i_n R_{film}\right)}{RT} \right) - \exp\left(\frac{-\alpha_c F\left(\Phi_1 - \Phi_2 - U - i_n R_{film}\right)}{RT} \right) \right] \qquad (3)$$

$$\varepsilon \frac{\partial c}{\partial t} = \nabla \cdot \varepsilon D \left(1 - \frac{d\ln c_o}{d\ln c} \right) \nabla c + \frac{t_-^o \nabla \cdot i_2 + i_2 \cdot \nabla t_-^o}{z_+ \nu_+ F_+} \qquad (4)$$

$$\frac{\partial c_s}{\partial t} = \frac{1}{r^2} \frac{\partial}{\partial r} \left(D_s r^2 \frac{\partial c_s}{\partial r} \right) \qquad (5)$$

$$I - i_2 = -\sigma \nabla \Phi_1 \qquad (6)$$

$$\nabla \Phi_2 = \frac{i_2}{k} + \frac{2RT}{F} \left(1 - t_+^o \right) \left(1 + \frac{d\ln f_\pm}{d\ln c} \right) \nabla \ln c \qquad (7)$$

$$\nabla \cdot i_2 = a i_n \qquad (8)$$

Equation 3, known as the Butler-Volmer equation, calculates the reaction rate per unit area of electrode interface. Equation 4 finds the Li^+ concentration in solution, which is dependent on the diffusion and the reaction at the electrode/electrolyte interface, using the concentrated solution theory and control volume formulation [13]. Equation 5 solves for the Li concentration on the electrode surface by approximating the electrode as a dispersion of uniform spheres and by using Duhamel's Superposition Integral [12]. Equation 6 is a direct interpretation of Ohm's law, used to find the solid phase potential, Φ_1, where I is the total current entering the node [A], i_2 is the current in the solution phase [A], and σ is the solid phase conductivity [S/m]. Equation 7 models the potential drop in solution caused by the current and conductivity in solution and the concentration overpotential [12]. Lastly, Equation 8 is the divergence of the current, which is equal to the reaction rate, i_n, multiplied by the active interfacial area per unit volume, a [1/m].

Thermodynamics

The electrochemical heat generation is generally modeled by Equation 9 [14],

$$\dot{Q} = I \left(U - V - T \frac{\partial U}{\partial T} \right) \qquad (9)$$

where T is temperature [K], I is the total current [A], V is the voltage across the cell [V], and U is the open circuit cell potential [V] [12]. This model accounts for the irreversible heat generation caused by the cell resistance $I(U-V)$, and for the reversible heat term due to the entropy of reaction. However, the model does neglect the contribution from the heat of mixing. The use of Equation 5 in the electrochemical model restricts the model from fully solving for the heat of mixing. The error caused by neglecting this term is considered to be negligible [12].

$$\dot{Q} = 0.5\left[\frac{(V_{x,y}-V_{x-1,y})^2}{R_{x-\frac{1}{2},y}} + \frac{(V_{x,y}-V_x+1,y)^2}{R_{x+\frac{1}{2},y}} + \frac{(V_{x,y}-V_x,y-1)^2}{R_{x,y-\frac{1}{2}}} + \frac{(V_{x,y}-V_x,y-1)^2}{R_{x,y+\frac{1}{2}}}\right] \quad (10)$$

$$\rho C_p \frac{\partial T}{\partial t} = k_x \frac{\partial^2 T}{\partial x^2} + k_y \frac{\partial^2 T}{\partial y^2} + k_z \frac{\partial^2 T}{\partial y^2} \quad (11)$$

$$k_x = k_y = \sum_{i=1}^{5} k_i f_i \quad (12)$$

$$\frac{1}{k_z} = \sum_{i=1}^{5} \frac{f_i}{k_i} \quad (13)$$

$$\dot{q}_{conv} = h(T_{node} - T_{amb}) \quad (14)$$

$$\dot{q}_{rad} = \sigma E\left(T_{node}^4 - T_{amb}^4\right) \quad (15)$$

Equation 10 models the resistive heating in the current collector, where $V_{x,y}$ is the current collector voltage at node (x,y) [V], and R is the local collector resistance [Ω]. The local temperature is updated based on the node's heat generation rate and heat transfer to the surroundings using Equations 11 through 15, where k is the thermal conductivity [W/m^2K], T is temperature [K], t is time [s], ρ is density [kg/m^3], and C_p is heat capacity [J/K]. Equation 12 is used to find the local effective thermal conductivity by taking the product of the volume fraction and the sum of the conductivity of each layer. Equation 13 expresses the effective thermal conductivity for the z direction. Lastly, Equations 14 and 15 calculate the convective and

11

radiative heat transfer to the surroundings, where q is the heat transfer rate, T_{node} is the node temperature [K], T_{amb} is the ambient temperature [K], h is the convective heat transfer coefficient [W/m^2K], E is the emissivity, and σ is the Stefan-Boltzmann constant. Note that this model does not account for the conductive heat losses to the surroundings. The numerical methods used to solve these equations are detailed in a later section.

Computational Battery Modeling

To properly simulate the flow field in cell casings, a robust computation fluid dynamics model is required with sufficient heat transfer algorithms to model the heat generated by the electrochemical process. Simply creating a uniform heat generation boundary condition on the surface of the cell casing may not adequately model batteries' heat generation profile. Additionally, the model will have to account for heat transfer between the different modules, as the location of each module relative to the whole package would affect the local rate of heat transfer.

The engineering simulation software, Star-CCM+, was selected for this study because of the included Battery Simulation Module (BSM), permitting a simultaneous thermal-fluidic modeling approach [7]. The battery modeling functions in Star-CCM+ allow for the simulation of lithium-ion batteries with either wound cylindrical cells or stacked prismatic cells. The simulation module is designed to work with imported battery models from the Battery Design Studio® (BDS) along with an electrical load profile. The battery module is then completed with virtual connector parts and region definitions for the battery material. Next, a volume around the battery module is created with a fluid continuum defined around the module to simulate coolant flow [7].

In addition to the BSM, CFD software called SolidWorks Flow Simulation was used. This CFD

software allows for rapid configuration changes and ease in solid modeling. Due to the difficulty

of configuring Star-CCM+ to simultaneously operate the battery and thermal/flow solvers, Flow

Simulation was used for the thermal analysis. Future work will involve modeling the entire

simulation in Star-CCM+, to take advantage of its integrated solver.

Solving Techniques

The Battery Simulation Module is capable of using three different models for battery heat

generation: the NTG (Newman, Tiedeman, Gu [15,16]) model, the RCR model, and the DISTNP

model. The NTG model uses a polynomial approximation to predict cell voltage of the given a

set of constants (a_0 through a_{10}) and the load profile. Equations 16 through 21 are the primary

governing formulae for the NTG model,

$$V_{cell}(DoD, J) = \frac{J}{Y} + U + b(T - T_{ref}) \tag{16}$$

$$DoD = \frac{\int Idt}{Capacity}, J = \frac{I}{A} \tag{17}$$

$$U = a_0 + a_1 DoD + a_2 DoD^2 + a_3 DoD^3 \tag{18}$$

$$Y = (a_4 + a_5 DoD + a_6 DoD^2)_e^{\frac{E_a}{R}\left(\frac{1}{T_{ref}}, \frac{1}{T}\right)} \tag{19}$$

$$\frac{dU}{dT} = a_7 + a_8 DoD + a_9 DoD^2 + a_{10} DoD^3 \tag{20}$$

$$Q = A \cdot \left(U - V_{cell} + T\frac{dU}{dT}\right) \tag{21}$$

where V_{cell} is the cell voltage [V], DoD is the fractional depth of discharge, Y is the conductance [S/m^2], U is the equilibrium voltage [V], J is the current density [A/m^2], A is the elctrode area [m^2], I is the current [A], T is the temperature [K], T_{ref} is the reference temperature [K], and Q is the electrode heat generation [W] [7,15,16]. Note that the BSM increases the accuracy of the original model by adding an activation energy term to Equation 19 to account for temperature effects. Overall, this model is best for constant discharge cells such as those in electric vehicles, but requires discharge curves for the battery cells to acquire the fit coefficients, which may prohibit its use in this study.

The RCR, or resistor-capacitor-resistor, model uses a simple RCR circuit constructed from a resistor and capacitor in parallel with another resistor in series to simulate the cell, as shown in Figure 2. This model allows for a faster behavior response due to the transient nature of the capacitor and as such, is better for simulating cells with high discharge peaks [17].
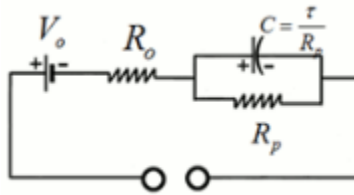

Figure 2. Equivalent circuit used in the RCR model for battery simulations. [7,17]

Equations 22 through 27 are the governing equations for the RCR model,

$$V_0 = \sum a_i \cdot SOC^j \tag{22}$$

$$R_o = e^{-\frac{E_o}{RT}} \sum R_{o,i} \cdot SOC^j, E_o = \sum E_{o,i} \cdot SOC^j \tag{23}$$

$$R_p = e^{-\frac{E_p}{RT}} \sum R_{p,i} \cdot SOC^j, E_p = \sum E_{p,i} \cdot SOC^j \tag{24}$$

14

$$\tau = e^{\frac{-E_\tau}{RT}} \sum \tau_i \cdot SOC^j, E_\tau = \sum E_{\tau,i} \cdot SOC^j \quad (25)$$

$$V_L = V_o - I \cdot R_o - \left(\frac{I}{C}\right)\Delta t + (V_L - V_o + I \cdot R_o)_{t-\Delta t} \exp\left[\frac{-\Delta t}{\tau}\right] \quad (26)$$

$$\frac{dV_o}{dT} = \sum \frac{dV_o}{dT_i} \cdot SOC^j \quad (27)$$

$$Q = I \cdot \left(V_o - V_L + T\frac{dV_o}{dT}\right) \quad (28)$$

where V_0 is the source voltage [V], V_L is the electrode voltage [V], SOC is the state of charge, R_n is a resistance [Ω], E_n is the energy capacity [J], τ is the time constant of the capacitor [s], I is the current [A], T is the temperature [K], and Q is the electrode heat generation [W].

Lastly, the DISTNP model is a fundamental electrochemistry model that can predict the performance of cells with many active materials and more accurately models the diffusion coefficients [18]. However, this model does require many input parameters to characterize the battery cell. Since the model is based on first principles and not numerical approximations, it is much more accurate and robust at the cost of set-up and computation time. The NTG method was selected for use in this study because of its balance of accuracy and speed.

SolidWorks Flow Simulation employs a finite volume method to solve the Navier-Stokes and conjugate heat transfer equations [19]. The meshes used in the finite volume method are rectangular in form and are refined in local regions near any solid/fluid interfaces. The solver approximates the spatial derivatives of the governing equations using implicit finite-difference methods of the second order. The time derivative terms are calculated using an implicit Euler method of the first order [19]. Figure 3 shows the rectangular meshing scheme that the solver uses.
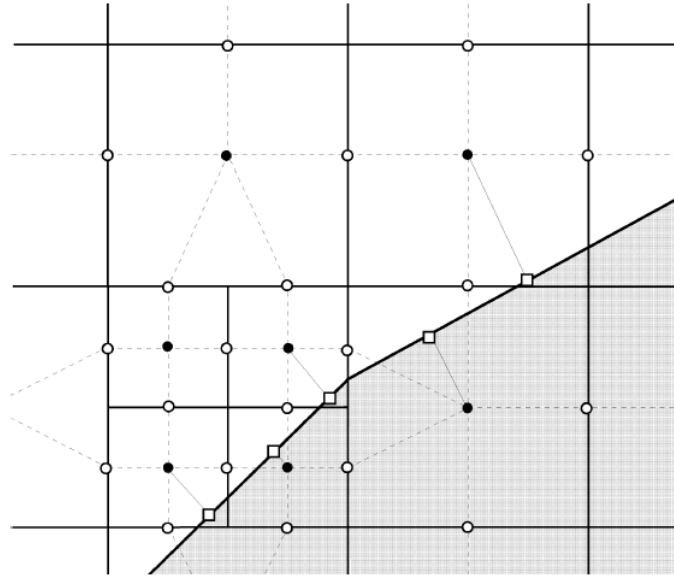
Figure 3. Rectangular-orthogonal meshing scheme employed by the finite difference solver in SolidWorks Flow Simulation [19].

Vortex Flow Characteristics

Coolant flow between each battery module can be modeled as a more simple flow between two parallel plates with a heat flux boundary condition that varies with location and time (or more specifically, charge/discharge rate). Under these conditions, the local heat transfer coefficient depends on the growth of the hydrodynamic and thermal boundary layers in the streamwise direction [20]. At a sufficient distance from the entrance region, the edge of the battery casing in this case, the boundary layers become fully developed, that is, the velocity and temperature profiles do not change greatly in the streamwise direction. Once this occurs, the heat transfer coefficient becomes a steady-state constant [20].

As previously mentioned, the benefit of promoting mixing in fluid channels in the context of increasing the local convective rate of heat transfer has been extensively studied [5]. If turbulence promoters in the form of transverse ribs are installed on the walls of the battery

16

module casings at a uniform spacing, it is expected that the heat transfer coefficient is prevented from reaching steady state because the flow's development is disrupted by the turbulence promoters. This development repeats for every section between sets of ribs, and as such, the velocity profile and shape of the temperature profile oscillate in each section. Despite this periodicity, the average heat transfer coefficient over the length of a ribbed wall is higher than in channels without ribs. This method however can be costly in terms of the head pressure required to achieve sufficient turbulence; a problem mitigated by the use of wing or winglet-type vortex generators (VGs), shown in Figure 4.
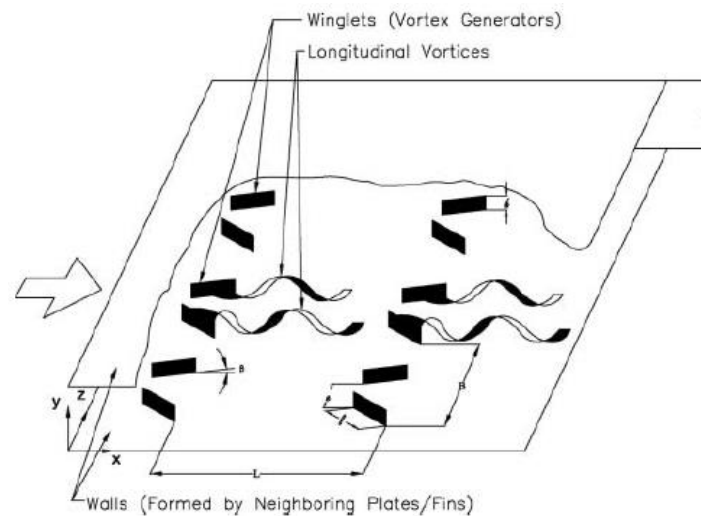

Figure 4. Generation of longitudinal vortices by winglet-type vortex generators [5].

Vortex generators differ from ribs in that VGs attempt to mix laminar flows by creating vortices instead of simply tripping the flow into turbulence. Some types of vortex generators are offset strip fins, louvered fins, wings, and winglets. Offset strip and louvered fins are commonly used in gas-liquid cross-flow heat exchangers but have a higher pressure loss than wing and winglet type VGs [5]. The wing and winglet type VGs use an angle of attack to induce longitudinal vortices, creating a swirling action in the wake of the wing as shown in Figure 4. This swirling

17

interrupts the growth of the boundary layer and increases the heat transfer coefficient without the high pressure cost of the rib design. These winglets can be triangular or rectangular in shape and can be welded on to or punched out of the heat transfer surface depending on the application.

Performance Factors

There is an inherent trade-off between heat transfer coefficient enhancement and head pressure. A primary factor in this exchange is the angle of attack of the winglets. It has been shown that pressure loss increases with increasing angle of attack and heat transfer begins to decrease after an angle of 55° for Reynolds numbers from 100 to 3000 [5]. Figure 5 shows flow field cross sections over a wing with an angle of attack of 20°. The cross sections clearly show the generation and deformation of the vortices as the flow progresses over the wing. The effect that angle of attack has on the mixing of the flow is shown in Figure 6. There is a significant increase in the average Nusselt number and thereby in the local heat transfer coefficient with the addition of a wing and with the increase in angle of attack [21].
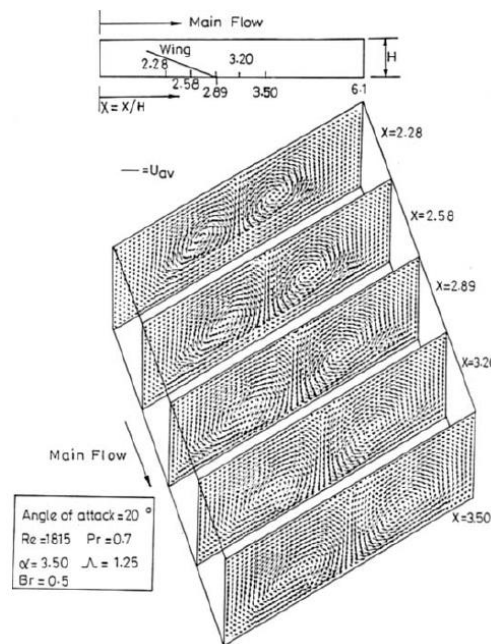

Figure 5. Generation and deterioration of wing-induced vortices in channel flow [21].
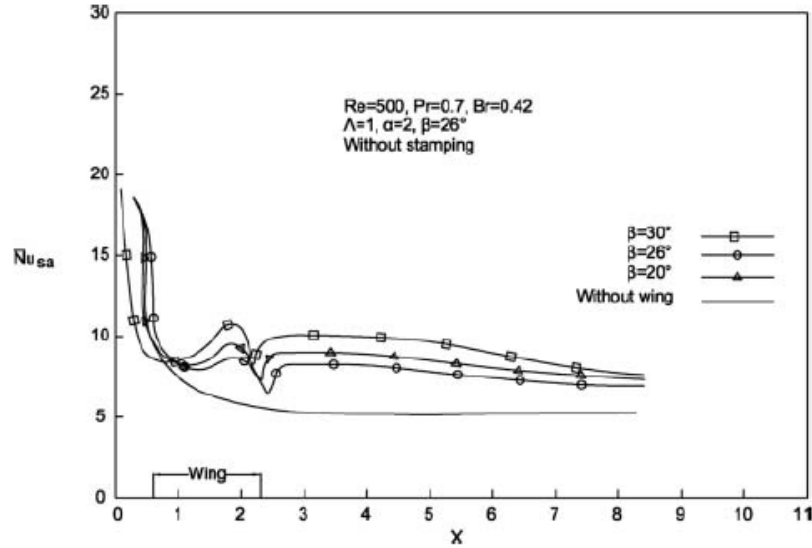
18

Figure 6. Spanwise average Nusselt number along the stream for varied angles of attack [5].

Simulation Configuration

The Chevrolet Volt battery pack was selected to simulate typical battery thermal conditions. The Volt is a plug-in hybrid electric vehicle that operates as a pure EV during the first 25-40 miles, during which the battery's charge is depleted [22]. Past a charge level threshold, the Volt's range-extending internal combustion engine (ICE) powers an electric generator that maintains the battery's charge [22].

The Volt battery pack has a 16 kWh capacity for the 2011 model year and weighs 435 lb. The pack consists of 288 pouch-type lithium ion cells that are approximately 5 inches in width, 7 inches in height and less than 1/4 inches in thickness [22]. The cells have $LiMn_2O_4$, or lithium-manganese-oxide chemistry, and are manufactured by Compact Power (CPI), a subsidiary of LG Chemical. The battery cells were modeled in BSM using the same chemistry with a discharge cycle of 3.75 volts, which is the nominal voltage for these cells [23]. Each pair of cells sandwiches an aluminum cooling fin that is stamped with five coolant flow tubes [24]. Because the flow tubes of these fins are so small, manufacturing them to contain winglets would greatly

19

increase their cost. Addtionally, the pressure cost associated with installing winglets into the tubes would offset the heat transfer benefit.

Instead, the BTMS design can be changed to a simple open channel with winglets welded to one wall of the fin, as shown in Figure 7. The flow channel model, shown in Figure 7, is based off the size of the li-ion cells used in the Chevy Volt. The winglets' size and orientations are shown in Figure 7 and have been selected based on the work of Biswas et al. [5]. Additionally, three horizontal and four vertical groups of winglets have been placed in the channel in an attempt to mitigate potential edging effects near the walls and leading edge. The flow channel is modeled using 6061 Aluminum alloy, which is comparable to the aluminum used in the Chevy Volt fin. The coolant used in the simulation is 50/50 Ethylene Glycol and Water mixture, which is commonly used in automotive radiators. The mass flow rate for the 50/50 Ethylene Glycol was selected as 0.05 kg/s, based on typical channel flow rates for plate heat exchangers [25].
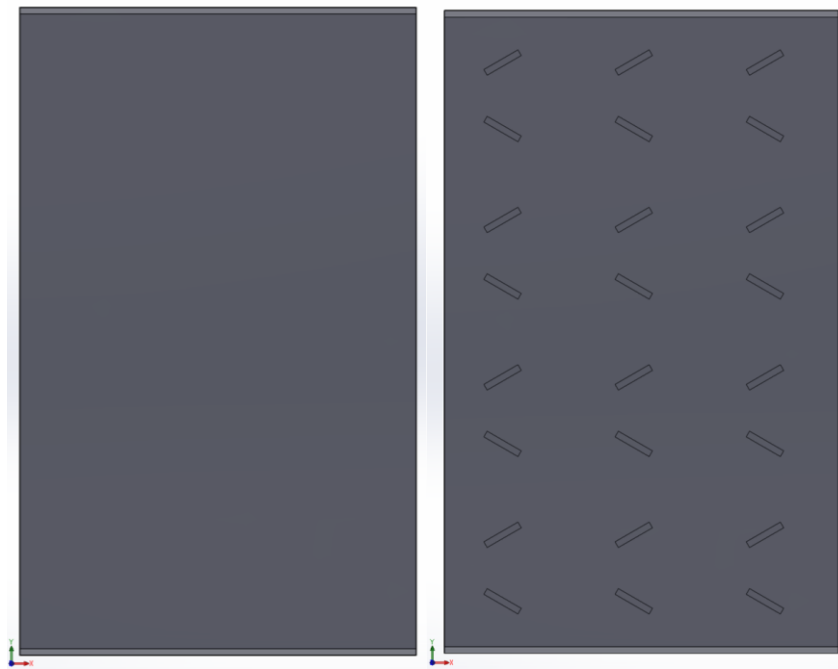

Figure 7. Aluminum cooling channel, without winglets installed (left) and with winglets installed (right).

CHAPTER III

RESULTS AND DISCUSSION

Cell Heat Generation

The volumetric heat generation of the li-ion cell is shown in Figure 8 for the specified chemistry and discharge profile, as computed by the BSM using the NTG method. The heat generation ranged from 12,600 W/m^3 at the base of the cell to nearly 17,500 W/m^3 near the contact tabs. This gradient of heat generation was expected to be concentrated near the tab roots because that is the area offering the least electrical resistance to discharge.
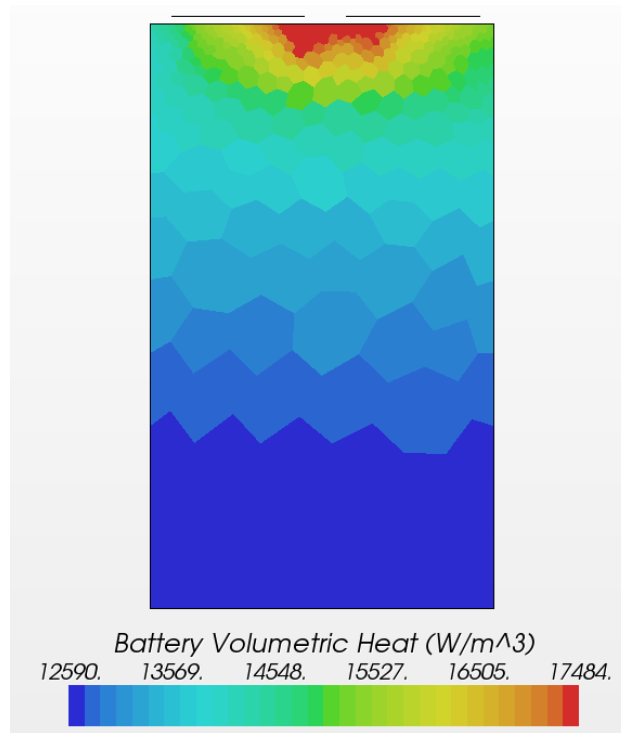

Figure 8. Simulated volumetric heat generation for one lithium-ion cell.

To better demonstrate the winglets' efffect on the convective heat transfer, the heat generation from each battery cell was taken to be a constant 20,000 W/m^3. This is a reasonable assumption

based on the heat generation model's results. A side effect of setting this parameter to be a constant is the decrease in computation time for each simulation. Based on a cell thickness of 6.126 mm (0.25 in), the surface heat flux on the outside surface of the aluminum channel would be 122.5 W/m^2. This surface flux was used as the boundary conditions for each outside wall of the channel. In addition to the heat generation from the battery, the environmental temperature was taken to be 318 K, a temperature typical of hot summer days in Phoenix, Arizona [26].

Vortex Generator Effects

The results of the flow simulation are shown in Figures 9 through 13 for both the nominal and winglet case. For each configuration, the inner wall temperature, center line fluid temperature, and inner wall heat transfer coefficient profiles are shown.
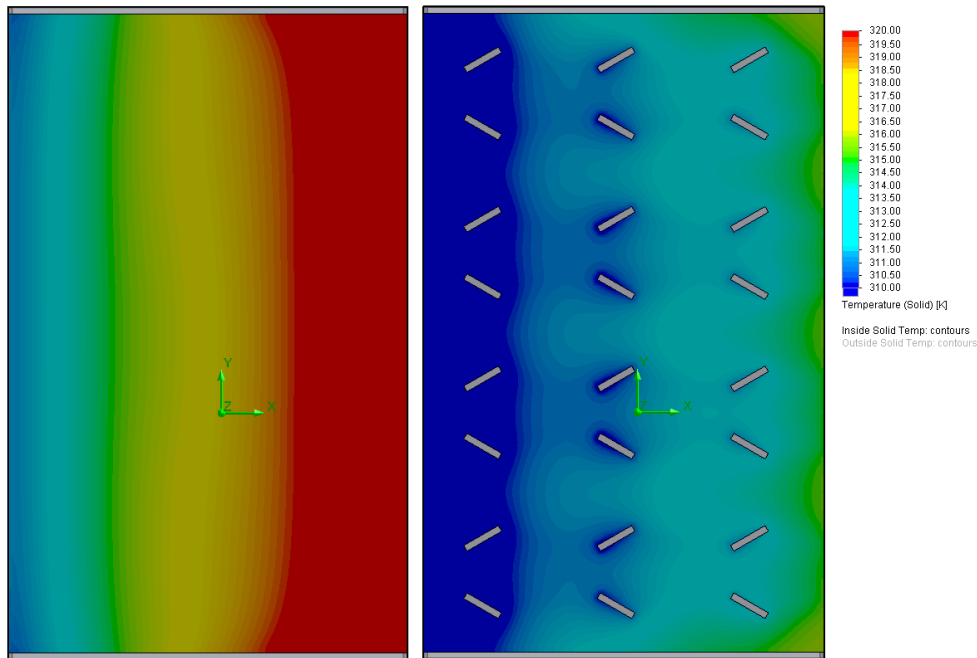

Figure 9. The inner channel wall temperature profiles for the nominal (left) and with winglet (right) case. Note that the scales are the same for both profiles and are shown in Kelvin.

As shown in Figure 9, the addition of the winglets into the flow field greatly decreases the average surface temperature on the inside wall from 317.4 K to 311.7 K. In addition, the temperature gradient in the x direction is more favorable with winglets when compared to the nominal case. The maximum temperature of the inside wall also decreases from 322.5 K to 316.18 K. The implication of these results is that by adding the winglets, a designer has a larger thermal ceiling to work with before reaching the threshold of around 320 K. This allows for cell chemistries with greater power densities, and therefore greater thermal power output to be used in electric vehicles. The larger thermal ceiling would also allow for the battery pack to be operated in warmer environments.
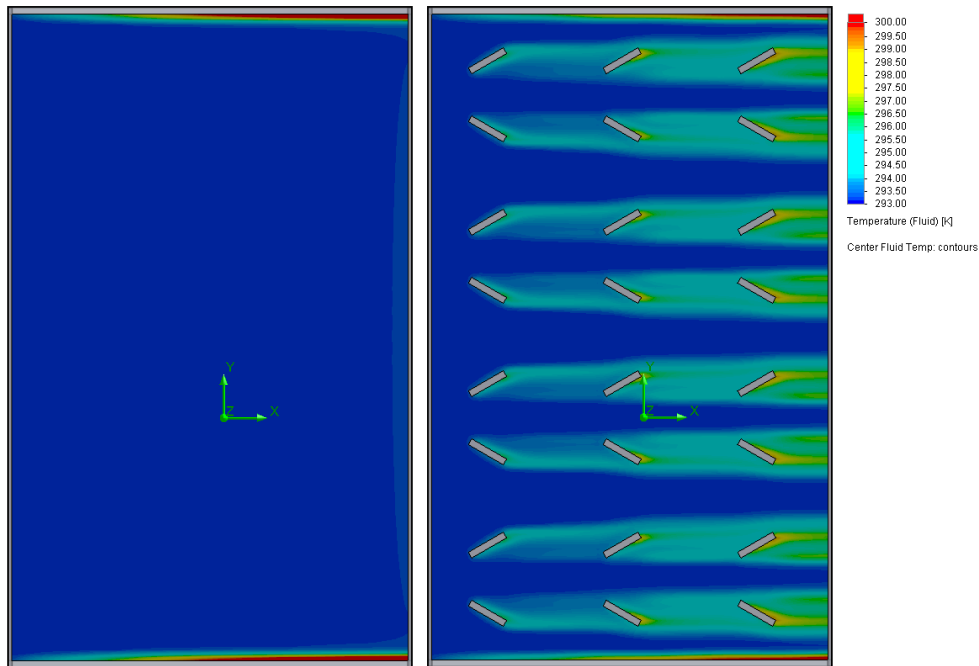

Figure 10. The center channel fluid temperature profiles for the nominal (left) and with winglet (right) case. Note that the scales are the same for both profiles and are shown in Kelvin.

Figure 10 shows the coolant temperature at the center (in the z direction) of the channel. The introduction of winglets into the channel causes an increase in the fluid temperature behind each of the winglets. This shows that the vortices generated by the winglets are increasing the local

laminar mixing, causing more thermal energy to transfer to the coolant, increasing its temperature behind the winglets. The claim that the winglets increase the local heat transfer is further supported by the convective heat transfer coefficient profile, shown in Figure 11.
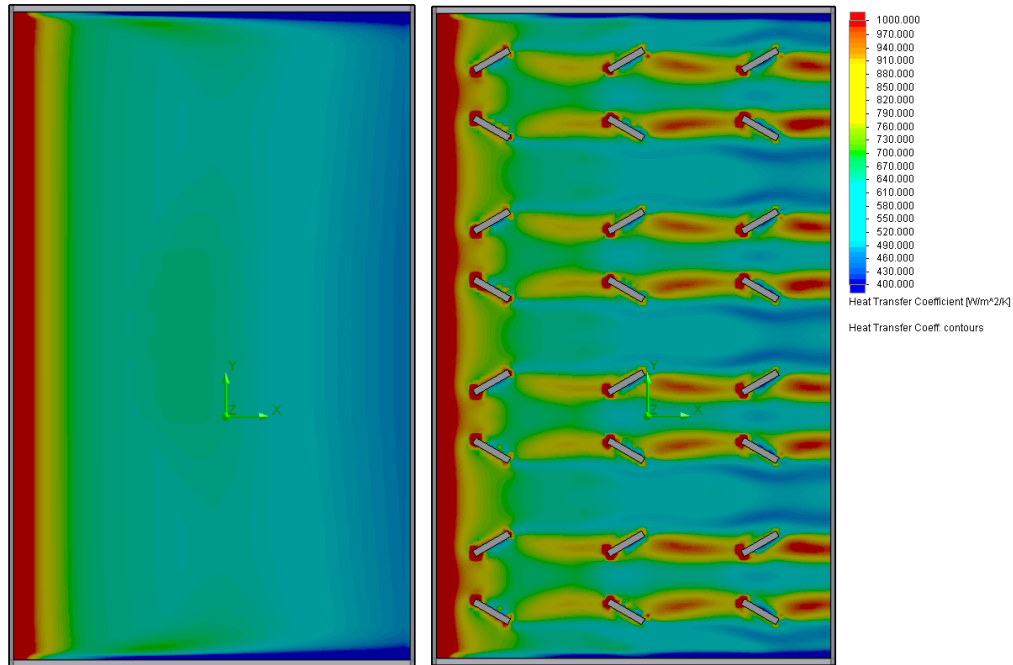

Figure 11. The convective heat transfer coefficient profiles for the nominal (left) and with winglet (right) case. Note that the scales are the same for both profiles and are shown in W/m²·K.

In the vortex region behind each winglet, it is apparent that the local convective heat transfer coefficient increased as compared to nominal. At the stagnation point in front of each winglet, there is a sharp increase in the local heat transfer coefficient. This is likely caused by small vortices forming at the front of the winglets. Additionally, in the wake of each winglet, where the vortices of the winglet laminarly mix the coolant, there is a significant increase in the heat transfer coefficient. The streamwise variation of the heat transfer coefficients is shown in Figure 12. The streamwise average heat transfer coefficient increases from 665 to 917 W/m² K with the addition of winglets into the channel. This 38% increase in convective heat transfer coefficient is directly caused by the increased level of laminar mixing occurring in the wake of the winglets.
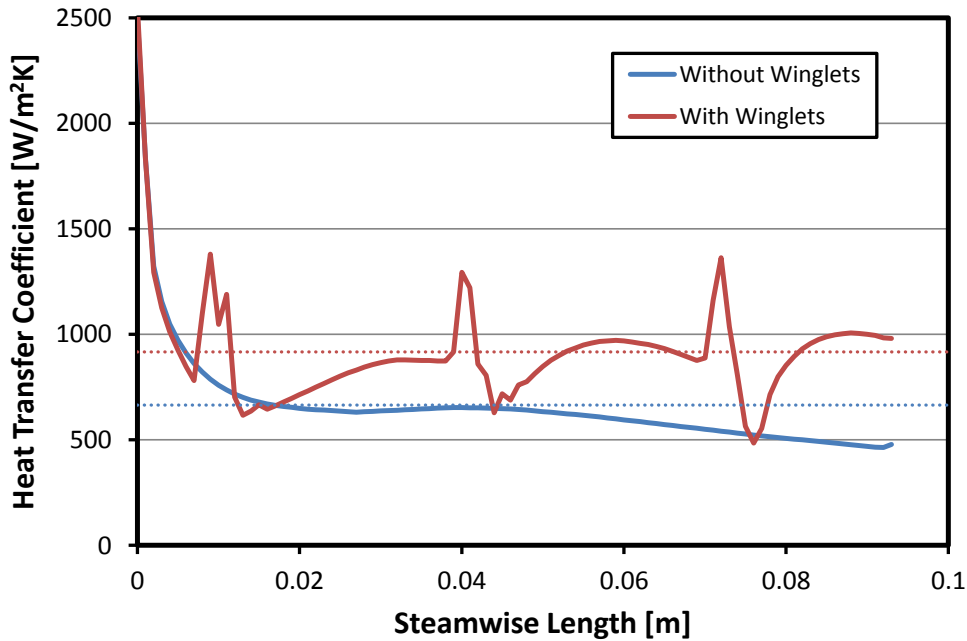
Figure 12. The local heat transfer coefficient along the streamwise length of the channel at the winglets (y = 3.5 in). Note that the dashed lines represent the average coefficient along the length.

Another variable of particular concern is the cost to pump the coolant. Pumping power is the product of pressure drop across the inlet to outlet, and the mass flow rate. Therefore, by looking at how the winglets affect the inlet to outlet pressure difference, their effects on pumping power can be determined without modeling the entire BTMS. The average pressure drop increased by 33.6% with the addition of winglets. While this increase may seem large, the magnitude of the pressure drop is small relative to the atmospheric pressure. Additionally, a more complete model may be required to determine if this increase in pressure drop is large relative to the pressure cost of the entire BTMS system. For example, if the required power to pump the coolant *to each* channel inlet is significantly greater than the power required to pump the coolant *through each* channel, than the increase in required power by the winglets is negligible. The effect that winglets have on the pressure cost of the entire BTMS system will have to be determined for each unique BTMS design.

CHAPTER IV

CONCLUSIONS

In the context of battery thermal management, vortex generators provide a viable solution to efficiently handle electrochemical thermal loads. In this study, the addition of winglets into channel-type battery fin has many benefits at a small pressure cost. Firstly, at a given flow rate, winglets lowered the average fin wall temperature by over 6 K, which allows for BTMS designs to accommodate battery chemistries with greater thermal and electrical power densities. Alternatively, this additional safety factor of 6 K would allow for battery packs of comparable power density to that which was tested to be operated in more extreme temperatures. In addition, the winglets also caused a more evenly distributed temperature gradient, which increases cell longevity and mitigates the potential for catastrophic failure of the cells. This study showed that the vortices generated in the wake of the winglets caused a 38% increase in the average convective heat transfer coefficient, which in turn leads to the decrease in surface temperatures. These benefits come at a cost of a 33% increase in pressure drop and therefore pumping power. However, a case by case thermal-fluid analysis of a BTMS design is needed to determine if this increase in pressure drop significantly outweighs the thermal management benefit.

REFERENCES

[1]   T. Bandhauer, G. Srinivas,T. Fuller, A Critical Review of Thermal Issues in Lithium-Ion Batteries, J. The Electrochemical Society 158 (2011)

[2]   R. Sabbah, R. Kizilel, J.R. Selman, S. Al-Hallaj, An alternative cooling system to enhance the safety of Li-ion battery packs, J. Power Sources 194 (2009)

[3]   R. Sabbah, R. Kizilel, J.R. Selman, S. Al-Hallaj, Active (air-cooled) vs. passive (PCM) thermal management of high power Li-ion packs: Limitation of temperature rise and uniformity of temperature distribution, J. Power Sources 182 (2008)

[4]   R. E. Gerver, J. P. Meyers, Three-Dimensional Modeling of Electrochemical Performance and Heat Generation of Lithium-Ion Batteries in Tabbed Planar Configurations, J. The Electrochemical Society 158 (2011)

[5]   G. Biswas, H. Chattopadhyay, A. Sinha, Augmentation of Heat Transfer by Creation of Streamwise Longitudinal Vortices Using Vortex Generators, Heat Transfer Engineering (2011)

[6]   M. Silberberg, Chemistry: The Molecular Nature of Matter and Change, 4th Ed. New York (NY): McGraw-Hill Education. p 935. (2006)

[7]   STAR-CCM+ User Guide, CD-Adapco, v. 7.04, pp.4762-4924

[8]   T. Reddy, Linden's Handbook of Batteries, 4th ed, Chapter 3, McGraw Hill (2011)

[9]   P. Albertus, E. J. Cairns, Batteries for Electric and Hybrid-Electric Vehicles, Annu. Rev. Chem. Biomol. Eng., p. 299–320 (2010)

[10]   R. Gerver, J, Meyers, Three-Dimensional Modeling of Electrochemical Performance and Heat Generation of Lithium-Ion Batteries in Tabbed Planar Configurations, J. The Electrochemical Soc, 158(7), (2011)

[11]   M. Doyle, T. F. Fuller, and J. Newman, Modeling of Galvanostatic Charge and Discharge of the Lithium/Polymer/Insertion Cell, J. Electrochem. Soc., Volume 140, 1526 (1993)

[12]   K. Thomas, J. Newman, and R. Darling, In Advances in Lithium-Ion Batteries, W. Schalkwijk and B. Scrosati, Editors, p. 345, Kluwer Academic Publishers, New York (2002)

[13]   C. M. Doyle, Ph.D. Dissertation, University of California, Berkeley (1995)

[14]   D. Bernardi, E. Pawlikowski, and J. Newman, A General Energy Balance for Battery Systems, J. Electrochem. Soc., 132, 5 (1985)

[15]   Newman, J. and Tiedeman, W. Potential and Current Distribution in Electrochemical Cells, J. Electrochem. Soc. 140(7), (1993).

[16]   H. Gu, Mathematical Analysis of a Zn / NiOOH Cell, J. Electrochem. Soc. 130(7) pp. 1459-1464 (1984)

[17]   Verbrugge, M. and Tate, E., Adaptive state of charge algorithm for nickel metal hydride batteries including hysteresis phenomena, J. Power Src. 126 pp. 236-249 (2004)

[18]   Fuller, T.F., Doyle, M.and Newman, Simulation and Optimization of the Dual Lithium Ion Insertion Cell, J. 1994. J. Electrochem. Soc., 141(1)

[19]   SolidWorks Flow Simulation 2012 Technical Reference Manual, Dassault Systèmes, pp. 48-53. (2012)

[20]   F. Incropera, D. DeWitt, Fundamentals of Mass and Heat Transfer, John Wiley & Sons, New York, NY, pp. 518-567. (2011)

[21]   G. Biswas, H. Chattopadhyay, Heat Transfer in a Channel with Built-In Wing-Type Vortex Generators, Int. J. Heat Mass Transfer, 35(4) pp. 803-814 (1992)

[22]   Chevrolet Volt Battery, Web, <http://media.gm.com/content/dam/Media/microsites/ product/volt/docs/battery_101.pdf> (2011)

[23]   R. DeMeis, Teardown Reveals Chevy Volt's Electronic Secrets, EDN Network, Web, <http://www.edn.com/design/analog/4372600/Teardown-reveals-Chevy-Volt-s-electronic-secrets>, (2012)

[24]   Cooling Fins Help Keep Chevrolet Volt Battery at Ideal Temperature, Web, http://media.gm.com/content/media/us/en/gm/news.detail.html/content/Pages/news/us/en/ 2011/Feb/0214_battery.html, (2011)

[25]   M. Fiebig, A. Valencia, N. K. Mitra, Wing-Type Vortex Generators for Fin-and-Tube Heat Exchangers, Experimental Thermal and Fluid Science, (1993)

[26]   "NowData - NOAA Online Weather Data". National Oceanic and Atmospheric Administration. <http://www.nws.noaa.gov/climate/xmacis.php?wfo=psr> (2013)